Improved optoacoustic microscopy through three-dimensional spatial impulse response synthetic aperture focusing technique

Jake Turner,[1,2] Héctor Estrada,[1] Moritz Kneipp,[1,3] and Daniel Razansky[1,3,*]

[1]*Institute for Biological and Medical Imaging, Helmholtz Zentrum München, Neuherberg, Germany*

[2]*Fakultät für Elektrotechnik und Informationstechnik, Technische Universität München, Munich, Germany*

[3]*Fakultät für Medizin, Technische Universität München, Munich, Germany*

**Corresponding author: daniel.razansky@helmholtz-muenchen.de*

Received January 29, 2014; revised April 2, 2014; accepted April 26, 2014;
posted April 30, 2014 (Doc. ID 205592); published June 3, 2014

Synthetic aperture focusing technique (SAFT) is effective in restoring lateral resolution of ultrasonic images for scans with focusing-related distortions. Although successfully applied in pulse-echo ultrasonics, the physical nature of an optoacoustic modality requires a modified algorithm to return accurate results. The SIR-SAFT method reported here uses the spatial impulse response (SIR) of the transducer to weight the contributions to the SAFT and is tailored to provide significant resolution and signal gains for out-of-focus sources in scanning optoacoustic microscopy systems. Furthermore, the SIR-SAFT is implemented in full three dimensions, applicable to signals both far of and at the focus of the ultrasonic detector. The method has been further shown to outperform conventional SAFT algorithms for both simulated and experimental optoacoustic data.

OCIS codes: (110.5120) Photoacoustic imaging; (110.0180) Microscopy; (110.7170) Ultrasound.
http://dx.doi.org/10.1364/OL.39.003390

In optoacoustic imaging absorption of short laser pulses by the imaged tissue induces a local temperature increase, which in turn leads to the generation of an acoustic wave. Thus, owing to the low acoustic scattering in soft biological tissues, optoacoustics can deliver images noninvasively and with diffraction-limited ultrasonic spatial resolution at depths ranging from several millimeters to centimeters in scattering tissues [1,2]. In high-resolution optoacoustic microscopy applications a single-element ultrasound transducer is typically scanned above the imaging target, whereas high lateral resolution of the measurement is achieved through either optical focusing [3] or, alternatively, acoustic focusing with a tightly focused transducer [4,5]. In the latter case, due to the high numerical aperture of the focused detector, only absorbing structures located close to the acoustic focus are resolved with high resolution, while the sources outside the tight acoustic focus are poorly laterally resolved.

The synthetic aperture focusing technique (SAFT) is generally effective in improving the lateral resolution of sources outside the acoustic focus, and the technique has been so far applied in ultrasound [6,7] and optoacoustic imaging [8], the latter is also known as the virtual detector approach [9]. SAFT is essentially a delay-and-sum based algorithm, and for pulse-echo ultrasound imaging (PE-US) the delays applied correspond to twice the time-of-flight for an acoustic wave from the detector surface to an acoustic scatterer [10]. It is assumed that distance is related to time of flight by $z = cN/f_s$, where c is speed of sound, N is sample number, and f_s is sampling frequency [7]. However, the application of SAFT to full optoacoustic microscopy data sets is partly flawed for two reasons. First, with send–receive modalities, such as PE-US, the spatial impulse response (SIR) of the transducer affects the strength of both generated and detected signals. Conversely, in the optoacoustic case the amplitude of signals emitted by sources is not governed by the properties of the ultrasonic transducer, which only influences the detected signals. Second, although conventional SAFT is effective far of the focus, it cannot be applied near to and at the focus because the filtering and averaging effects detrimentally alter the in-focus data. As a result, the data from within the focal area can only be restored if simply manually overlaid onto the final image alongside the results of SAFT [9]. A possible yet computationally and memory-intensive alternative to SAFT, in terms of improving out-of-focus optoacoustic data, is the model-based inversion that first numerically represents the forward problem of optoacoustic signal detection by the model matrix and then inverts the forward model matrix to attain the initial distribution of laser energy deposition in the imaged volume [11,12].

Here we present a modified algorithm based on the SIR of the ultrasound detector, SIR-SAFT, which provides significantly improved resolution and signal gains for out-of-focus sources in optoacoustic microscopy systems. Further, the SIR-SAFT implemented three dimensionally is applicable to both far of and at the acoustic focus and is computationally fast due to its simple delay-and-sum nature.

Since in optoacoustics there is no incident acoustic wave, the delays are half that of a pulse-echo system; the time-of-flight is from a source to the detector surface. As such, the modified delay, Δt, expression is given as

$$\Delta t = \mathrm{sgn}(t - t_f)(t_r' - t_r) = \begin{cases} < 0, & \text{if } t < t_f, \\ = 0, & \text{if } t = t_f, \\ > 0 & \text{if } t > t_f, \end{cases} \quad (1)$$

where sgn is the signum function, t is the time corresponding to the depth of the source as approximated by $z = cN/f_s$, and t_f is the time corresponding to the

approximated focal depth; t_r and t_r' are the approximated focal-depth to source and focal-point to source times of flight, respectively, where $t_r'^2 = x^2 + t_r^2$ and x is the lateral focus-source separation. The 1D SAFT summation applied elsewhere to optoacoustic imaging was otherwise unchanged from the PE-US application [7,9] and is given as

$$S_{\mathrm{SAFT}}(t) = \Sigma_{i=0}^{w-1} S(i, t - \Delta t), \tag{2}$$

where $S(i,t)$ is the signal recorded at scan position i and w is the extent of the summation. Rewriting for the three discretized dimensions (x_n, y_m, t), using Einstein summation notation and replacing the different values of w with a binary weighting mask $W_{nmij}(t)$, Eq. (2) becomes

$$S_{nm}(t) = W_{nmij}(t) D_{ij}(t - \Delta t), \tag{3}$$

where $D_{ij}(t - \Delta t)$ is the delayed time-domain signal acquired at transducer position $\mathbf{r}_{ij} = (x_i, y_j)$, and $W_{nmij}(t)$ is a weighting function at $\mathbf{r}'_{nmij} = (x_n - x_i, y_m - y_j)$, which is equal to 1 inside the focal-cone (Fig. 1) determined by the geometrical focusing of the detector and is 0 elsewhere.

The main error that arises in applying SAFT as per Eq. (2) directly to optoacoustics is in the nature of the extent-variable w, which varies with distance from the detector surface. Near the detector or deep of the focus, the angular extent of the detector gives a large set of contributions to the summation, i.e., w is a larger value. Conversely, nearer the focus, w is smaller. For PE-US the energy incident upon the scatterer is proportional to w at that depth. As such, when applying the summation in Eq. (3) to identical scatterers at different depths with the aforementioned binary contribution map $W_{nmij}(t)$, the signal amplitudes should be correctly rectified, i.e., either a small number of contributions of high amplitude or a large number of contributions of a smaller amplitude. However, for optoacoustic sources the generation of pressure waves is not dependant on the transducer and its SIR, while their detection is. The method proposed here uses a model of the SIR of the detector as a non-binary weighting mask $W_{nmij}(t)$, which accounts for the varying number of contributions but fixed amplitudes from equal optoacoustic sources at different depths. Additionally, the very same method can be applied throughout the dataset without the need for defining a near-focus region.

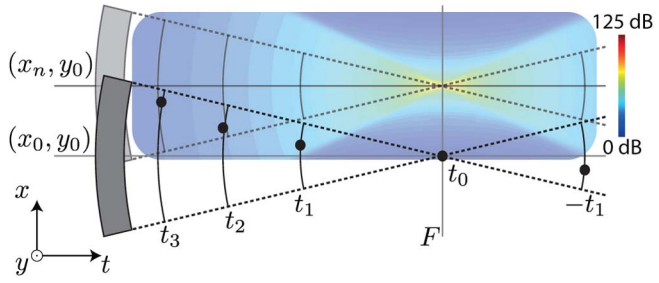

Fig. 1. Schematic of five acoustic sources at different depths from the focus, F, of the ultrasound transducer, with lines of equal-delay marked for each source. Two transducer positions, (x_0, y_0) and (x_n, y_0), are shown; position (x_n, y_0) has the central slice of $W_{nmij}(t)$ underlaid.

An illustration of SIR-SAFT is seen in Fig. 1. Five optoacoustic point sources have been placed at an arbitrary distance from the focal plane (F) of the transducer with the equal-delay arcs marked for each source (from $-t_1$ to t_3). Two positions for the spherically focused transducer are shown, $(x_0; y_0)$ and $(x_n; y_0)$, and the sources at t_2 and t_3 will also be detected by transducer position $(x_n; y_0)$; position $(x_n; y_0)$ has the central slice of $W_{nmij}(t)$ underlaid.

Overall, SAFT is known to improve the lateral resolution and increases the amplitude of out of focus signals, while improving SNR [6]. However, the edge of the extent of the contributions considered can cause artefacts in the output image. To address this issue, the contributions are often subject to a windowing function during SAFT [7] or a further post-beam forming step, namely the coherence factor (CF), to improve ultrasound images further still [13]. The CF is defined as

$$\mathrm{CF}_{nm}(t) = \frac{|S_{nm}(t)|^2}{N(t)(W_{mnij}(t)|D_{ij}(t - \Delta t)|)^2}, \tag{4}$$

where $N(t)$ is the depth-dependant nonzero width of $W_{nmij}(t)$, and $CF_{nm}(t)$ is effectively a measure of the phase relation of adjacent signals. However, the CF is sensitive to noisy data [7,9,13,14], which can be common in optoacoustic microscopy. Here we test SIR-SAFT both alone and in combination with the CF.

SIR-SAFT was subsequently tested with a simulated optoacoustic dataset obtained from 41 absorbing microspheres of 60 μm diameter uniformly spaced on both sides of the acoustic focus. Homogeneous illumination of short duration (<10 ns) was further assumed for simplicity, with pressure signals for the microspheres calculated according to [15]. A superposition of nine of the simulations is presented in the sinogram in Fig. 2(a). For detection, a spherically focused piezoelectric ultrasound transducer was assumed with a center frequency of 25 MHz, 60% available bandwidth, an outer diameter of 11 mm, and a focal length of 12.3 mm.

An experimental measure of the electrical impulse response (EIR) of the transducer was made using a 10 μm sphere [16], which was then used to simulate the SIR of the detector with the *Field II* software package [17]. The EIR was then used as the coefficients for a finite impulse response (FIR) filter, effectively convolving the simulated signals with the EIR of the modeled transducer. Additionally, Gaussian noise was added with an amplitude of 15% of the maxima. The simulations and processing were performed in 2D, and SIR-SAFT was also tested on an experimental data set in 3D.

The abilities of SAFT and SIR-SAFT to improve SNR and to resolve out-of-focus sources can be seen qualitatively in Fig. 2(a), which presents a section of the sinogram (raw data) of the simulated data set, and Figs. 2(b)–2(e) contain results of SAFT-based processing. It is readily observable that the images obtained with SIR-SAFT [Fig. 2(c)] and CF-SIR-SAFT [Fig. 2(e)] are the most effective at improving the lateral resolution of sources at all depths while also more accurately

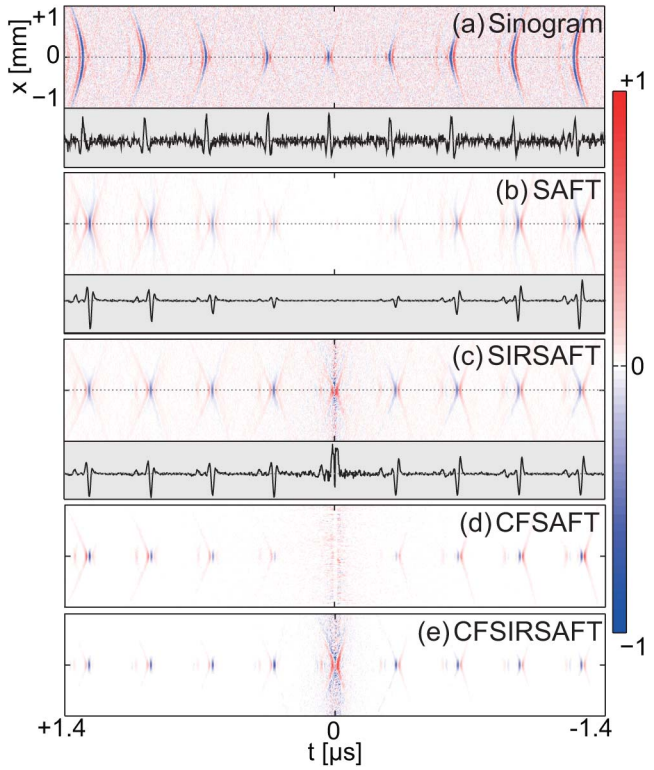

Fig. 2. (a) Superposition image of the sinogram for the simulated data (nine spheres shown). (b)–(e) Results of applying the different methods. (a)–(c) also present acoustic signals at $x = 0$ immediately below.

rectifying the signals. The values of FWHM and SNR for three of the sources in the simulated data and the subsequent SAFT-based processing results are presented in Table 1. The sources selected were located at the focus ($z = 0$ mm, $t = 0$ μs) and approximately ±3 mm of the focus ($t = \pm 2$ μs). Missing values in Table 1 denote measurements for which the SNR was too low to arrive at meaningful FWHM measures.

While with conventional SAFT the data from the focal area can only be restored artificially by copy-pasting the sinogram into the final image alongside the SAFT results, tests of the simulated data show that SIR-SAFT can seamlessly rectify the signals at all depths [Fig. 2(c)] rather than introduce large amplification for out-of-focus signals at the expense of those near the focus [Fig. 2(b)].

Table 1. Measures of Resolution (FWHM [μm] Lateral/Axial) and SNR (dB) Performance for SAFT, SIR-SAFT, CF-SAFT, and CF-SIR-SAFT[a]

	Source-Focus Time of Flight					
	−2 μs		0 μs		+2 μs	
Method	FWHM	SNR	FWHM	SNR	FWHM	SNR
Sinogram	638/27	13.4	207/24	13.8	518/27	13.7
SAFT	243/27	26.5	-/-	—	239/26	25.1
SIR-SAFT	225/27	36.1	152/7	39.2	224/26	36
CF-SAFT	167/24	64.7	-/-	—	158/24	65.9
CF-SIR-SAFT	169/25	75.3	152/7	81.8	160/25	75.2

[a]Values are for the three sources at the focus ($t = 0$) and ±2 μs from the focus.

Further, SIR-SAFT can be seen to outperform conventional SAFT in terms of improved lateral resolution, where the improvement compared to SAFT is small out-of-focus but significant for near-focus sources (Table 1). The performance of SIR-SAFT in improving SNR is also significant, with the rectified signals being of around 36–39 dB for all depths (Table 1), whereas conventional SAFT performed closely to SIR-SAFT out-of-focus but very poorly near-focus. Last, SIR-SAFT did not impede use of the CF, but rather the improvements were compounded. This is clearly seen as the results of CF-SIR-SAFT gave an SNR of >70 dB throughout the focal field, compared with 15 dB for the raw data (Table 1).

Experimental validation consisted of an optoacoustic microscopy dataset recorded from a 30 μm diameter suture loosely knotted and placed in clear agar with a layer of scattering agar (1% intralipid) above; the suture was at an oblique angle to the focal plane. A custom-made spherically focused 25 MHz piezoelectric ultrasound transducer (InSensor, Kvistgaard, DK) used for the experiments had the same geometry as in the simulations. Volumetric data were acquired using a variation on a fast scanning optoacoustic microscopy system [18], with broad illumination provided by a stationary fluid-filled light guide (Lumatec, Deisenhofen, DE). Distance between the adjacent scanning positions was 20 μm in both dimensions. Post-acquisition, the data were bandpass filtered between 3 and 30 MHz and down-sampled to 62.5 MS/s and 40 μm step size so as to reduce the computational burden.

A top-down photograph of the suture without the scattering layer [Fig. 3(a)] shows the approximate region of interest (ROI) for the acquired images as a white box. The maximum amplitude projection (MAP) images were produced for the sinogram [Fig. 3(b)], the results of conventional SAFT [Fig. 3(c)] and SIR-SAFT processing [Fig. 3(d)], and the subsequent application of the CF to both SAFT and SIR-SAFT [Figs. 3(e) and 3(f)]. The images are annotated with two white lines along which the FWHM of the suture was calculated. The lines correspond to a near- and far-focal depth (lower-left and upper-right, respectively). Note that the upper-right measure of FWHM for the sinogram [Fig. 3(b)] should be considered abstract given the lack of apparent structure.

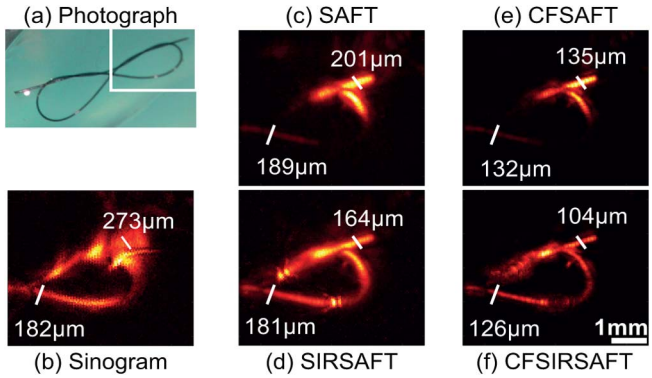

Fig. 3. MAP images with annotated measures of FWHM for a 30 μm suture orientated obliquely to the focal plane after different SAFT-based processing; a photograph of the suture phantom (without the scattering layer) is annotated with the approximate ROI.

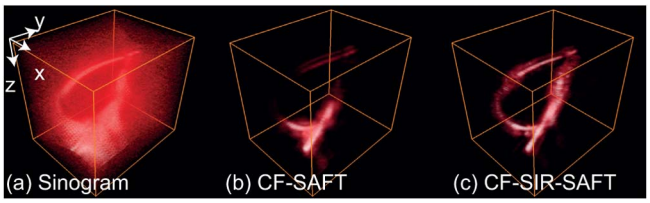

Fig. 4. Volume rendering of experimental optoacoustic microscopy data of a loosely knotted 30 μm suture for (a) the sinogram, (b) results of CF-SAFT processing, and (c) the results of CF-SIR-SAFT processing.

The sinogram for the experimental data and for the results of CF-SAFT and CF-SIR-SAFT processing were also rendered as volumes using Amira (Visage Imaging Inc.), which are presented in Fig. 4. In these images the data were normalized and the same colormap and thresholds were applied to each data set.

Overall, the testing of SIR-SAFT on the experimental data showed significantly better performance as compared to the conventional SAFT; again the performance was compounded by the application of the CF. This can be seen as the improvement of measurable FWHM of the suture both near and far of the focus (Fig. 3) and as the more uniformly amplitude-corrected suture structure throughout the rendered volume (Fig. 4).

The SIR-SAFT algorithm showcased here demonstrates the necessity of modifying the conventional SAFT algorithm used in ultrasonics beyond just the delay terms for useful application to optoacoustics. This is clear through the demonstrated ability to recover resolution and increase SNR without distorting the data, a highly desirable trait in acoustic resolution optoacoustic microscopy applications, especially as an accurate preprocessing technique pertaining to multispectral imaging and functional studies. Future work may consider nonuniform fluence in optical and acoustic resolution optoacoustic microscopy.

The research leading to these results has received funding from the European Union under grant agreement *ERC-2010-StG-260991*. The authors also acknowledge C. Lutzweiler for his helpful input.

References

1. V. Ntziachristos, Nat. Methods **7**, 603 (2010).
2. L. V. Wang, Nat. Photonics **3**, 503 (2009).
3. K. Maslov, H. F. Zhang, S. Hu, and L. V. Wang, Opt. Lett. **33**, 929 (2008).
4. S.-L. Chen, Z. Xie, L. J. Guo, and X. Wang, Photoacoustics **1**, 30 (2013).
5. R. Ma, S. Söntges, S. Shoham, V. Ntziachristos, and D. Razansky, Biomed. Opt. Express **3**, 1724 (2012).
6. C. Frazier and W. O'Brien, IEEE Trans. Ultrason. Ferroelectr. Freq. Control **45**, 196 (1998).
7. M.-L. Li, W.-J. Guan, and P.-C. Li, IEEE Trans. Ultrason. Ferroelectr. Freq. Control **51**, 63 (2004).
8. Z. Deng, X. Yang, H. Gong, and Q. Luo, Opt. Express **20**, 7555 (2012).
9. M.-L. Li, H. F. Zhang, K. Maslov, G. Stoica, and L. V. Wang, Opt. Lett. **31**, 474 (2006).
10. K. Langenberg, M. Berger, T. Kreutter, K. Mayer, and V. Schmitz, NDT Int. **19**, 177 (1986).
11. M. Ángel Araque Caballero, A. Rosenthal, J. Gateau, D. Razansky, and V. Ntziachristos, Opt. Lett. **37**, 4080 (2012).
12. J. Aguirre, A. Giannoula, T. Minagawa, L. Funk, P. Turon, and T. Durduran, Biomed. Opt. Express **4**, 2813 (2013).
13. C. Nilsen and S. Holm, IEEE Trans. Ultrason. Ferroelectr. Freq. Control **57**, 1329 (2010).
14. M.-L. Li, H. F. Zhang, K. Maslov, G. Stoica, and L. V. Wang, Proc. SPIE **6086**, 60861F (2006).
15. A. Rosenthal, D. Razansky, and V. Ntziachristos, IEEE Trans. Med. Imaging **29**, 1275 (2010).
16. M. A. A. Caballero, A. Rosenthal, A. Buehler, D. Razansky, and V. Ntziachristos, IEEE Trans. Ultrason. Ferroelectr. Freq. Control **60**, 1234 (2013).
17. J. A. Jensen, in *10th Nordicbaltic Conference on Biomedical Imaging* (1996), Vol. **4**, pp. 351–353.
18. H. Estrada, J. Turner, M. Kneipp, and D. Razansky, Laser Phys. Lett. **11**, 045601 (2014).